Chapter 5

Diffuse far-ultraviolet emission in 30 Doradus in the Large Magellanic Cloud

5.1 Introduction

The *FUSE* telescope has observed diffuse FUV emissions across different regions within the Large Magellanic Cloud (LMC). These emissions exhibit intensities ranging from 1000 to 3×10^5 photon units. Among these regions are the prominent H II regions within the LMC, namely 30 Doradus and N11. Known as the most active star-forming region in the Local Group, 30 Doradus stands out with the highest reddening in the LMC. This chapter is dedicated to modeling the diffuse FUV emissions originating from the 30 Doradus H II region, aiming to explore and understand the region's dust scattering characteristics.

5.2 The Large Magellanic Cloud and 30 Doradus

The LMC presents an advantageous laboratory for scrutinizing the impact of massive stars on dust characteristics. Its nearly face-on orientation minimizes confusion and extinction along the galactic plane. Known to be approximately 50 kpc away [184], the LMC facilitates the resolution and comprehensive study of stars alongside interstellar gas and dust [185]. Situated at a high latitude of about 30°[186] , it experiences minimal obstruction from extinction caused by the Milky Way dust. Hence, the LMC has been a prime target for various space-based observatories, aimed at exploring dust properties and establishing calibrated dust emissions as indicators of star formation.

The 30 Doradus, also referred to as the Tarantula Nebula, stands out as the brightest and most active star-forming H II region in the galactic neighborhood, situated in the LMC. At the heart of this region lies the significant RMC 136 star cluster, hosting numerous young, high-mass ionizing stars. A comprehensive study of dust scattering and emissions in this H II region holds immense significance, contributing to a comprehensive understanding of the distinctive dust characteristics prevalent in the LMC.

Multiple investigations have delved into the 30 Doradus and its immediate vicinity, unraveling insights into the ISM and the mechanisms of star formation. Moreover, extensive research has scrutinized the diffuse emission present in the LMC, spanning various wavelengths encompassing radio, optical, FUV, and X-rays. [187] observed distinctive reddening in stars near the 30 Doradus core within the LMC, attributing it to a nebular-type extinction law, while the rest of the LMC adhered to standard extinction laws, giving rise to the "two-component model". [11] provided an extensive discussion on dust grains within the diffuse ISM of the Milky Way and Magellanic Clouds, covering aspects like size, composition, shape, formation, evolution, and model extinction curves. [96] investigated the diffuse FUV emission in the LMC and associated them with small carbonaceous and silicate grains. [188], using *Spitzer* observations (SAGE [189]), identified a MIR and FIR excess in the LMC linked respectively to dust distribution and undetected CO gas, later confirmed by [190]. [97] compared FUV diffuse emission observed by *FUSE* with MIR and FIR emissions in the two H II regions, revealing a strong UV - IR correlation. [191] significantly contributed to 30 Doradus nebula research, discussing the formation of young massive stars and highlighting the nebula's dynamic nature. [192] detected 299 candidate young stellar objects in 30 Doradus, noting a 40% higher star formation threshold compared to the Milky Way. [193] and [194] examined dust polarization degree variations, magnetic field morphology, and strength in 30 Doradus using SOFIA observations. [195] derived the reddening vector direction and extinction law in 30 Doradus. [196] observed discrepancies in standard models used for our galaxy in explaining certain types of dust light, emphasizing the potential role of small dust particles, especially in energetic regions. Lastly, [197] identified strong spatial gradients in extinction properties across RMC 136's core, coinciding with a density gradient in cold gas.

As mentioned earlier, [97] studied the correlation between UV and IR diffuse emissions from 30 Doradus, employing data from the *FUSE* telescope. In this work, our focus lies in modeling the diffuse FUV emission of the dust scattered starlight at specific locations within the 30 Doradus H II region of the LMC. Our aims encompass understanding the optical behaviors of dust, particularly its scattering and attenuation optical depths, alongside its

extinction properties. Prior investigations have explored extinction laws for the 30 Doradus nebula in the NIR and optical wavelengths [198]. Recent research has extended these studies to the UV range [197]. However, for a more comprehensive understanding, we strive to expand these extinction laws into the FUV realm. The primary UV emission originates from the ionizing star cluster RMC 136, centrally located within the 30 Doradus region. To achieve our objectives, we employ the single-scattering dust model [95], which was previously utilized in the preceding chapter.

5.3 Observations and data analysis

In our investigation, we base our modeling of scattered FUV intensities on observations carried out by [96] using the *FUSE* telescope within the LMC. These observations encompass seven distinct wavelength bands, spanning from 1004 Å (1A1) to 1159 Å (2A1), covering a total of 81 dust locations across the LMC, with seven situated within the 30 Doradus H II region (Table 5.3). Among these locations, one (L1) resides near the RMC 136 cluster, while the remaining six (L2-L7) form a cluster surrounding the SN1987A supernova remnant (refer to Fig. 5.1). To construct our dust model, we extract the observed surface brightness of diffuse radiation captured by *FUSE* from Table 1 in the work of [96]. The values for scattering albedo (α), asymmetry factor (g), and extinction cross-section (σ_{ext}) for typical LMC dust are adopted from the study by [35].

5.3.1 The model and input parameters

We employed the single scattering model as we used in the previous chapter. A description and justification of using the model has been given in Sec. 4.4.1 in Chapter 4. Here, we discuss about the different input parameters required for the modelling in our concerned region.

Neutral and Molecular Hydrogen Map of 30-Doradus

The 30 Doradus H II region demonstrates weak aromatic dust emission features from both molecular and atomic hydrogen [199]. About 10% of the studied area exhibits CO line emissions, reaching temperatures peaking at around 0.15 K, largely originating from extensive molecular clouds extending roughly 2400 pc south of 30 Doradus. Additionally, within this region, a prominent high-velocity CO component suggests molecular material acceleration driven by stellar winds, supernovae, or a combination thereof [199]. Estimates

indicate a total molecular cloud mass in the LMC of $1.4 \times 10^8 M_{\odot}$. The transition from atomic to molecular hydrogen occurs within the density range of $N(H) = 4 \times 10^{21}$ cm^{-2} to $N(H) = 6 \times 10^{21}$ cm^{-2} [200]. Notably, a substantial portion (70% - 90%) of H_2 within the 30 Doradus area lacks CO, with comparatively faint CO lines compared to the Milky Way. This necessitates a CO-H_2 conversion factor ($X_{CO} = (1 \sim 4) \times 10^{21}$ cm^{-2}) [190, 201]. Hence, in calculating $N(H)$, the contributions of both atomic and molecular hydrogen are essential. To theoretically compute the intrinsic total hydrogen column density $N(H)$ along the line of sight towards 30 Doradus, we employ the formula from previous studies [202, 203]:

$$\frac{E(B-V)}{N(H)} = 4.5 \times 10^{-23} cm^2/H \tag{5.1}$$

Taking $E(B-V) = 0.29$ for 30 Doradus and $E(B-V) = 0.18$ [204] for SN 1987A, we determine $N(H)_{30Dor} = 6.44 \times 10^{21}$ cm^{-2} and $N(H)_{SN1987A} = 4 \times 10^{21}$ cm^{-2}. However, for a more comprehensive hydrogen map, we integrate various HI and H_2 surveys to approximate an average value for $N(H)$ (refer to Table 5.1). Utilizing the AIfA HI Surveys Data Server and HEASARC N(H) tool, which offer HI and H_2 profiles from surveys such as HI4PI [205–207], GASS [208], and LAB [209, 210], we extract precise H profiles for RMC 136 complex and SN1987A. The average $N(H)$ value in the line of sight, including the Milky Way, approximates $5 \sim 5.5 \times 10^{21}$ cm^{-2} for RMC 136 and $3.3 \sim 4 \times 10^{21}$ cm^{-2} for SN1987A. This leads to a rough estimate of mean $N(H)$ in the line of sight for the entire 30 Doradus H II region at 4.5×10^{21} cm^{-2}.

Table 5.1 Total hydrogen column density N(H) map of 30 Doradus and SN1987A. N(H) is in the units of H atoms per cm^2 [Credits: AIfA Hi Surveys Data Server of the Argelander-Institut für Astronomie and HEASARC N(H) tool]

Name	-	RMC 136	SN1987A
Latitude	l(°)	279.465	279.703
Longitude	b(°)	-31.67	-31.937
GASIII	0.266° beam	4.8E+21	2.9E+21
HI4PI Gaussians HI	Effective beam	5.0E+21	3.1E+21
HI4PI Gaussians H2	Effective beam	5.3E+19	0.9E+19

Star Locations and Luminosity

In our FUV scattering model, we focused on the highly massive young O and B-type stars residing in the central star cluster, RMC 136, situated within the core of 30 Doradus, as well as near the vicinity of SN1987A. For simplicity in modeling the dust properties, we

treated the entirety of the star cluster RMC 136, comprising more than 1100 young ionizing stars, as a unified giant radiation source with an average intrinsic luminosity. [191] described this stellar population at the heart of 30 Doradus, identifying approximately 1100 early-type massive stars through spectroscopic analysis. Their cumulative ionizing Lyman continuum output, stemming from 1170 massive stars within a 150 pc radius of RMC 136, approximates 1.25×10^{51} photons/s, leading us to model RMC 136 as a single O7V type star, with the combined UV luminosity of these 1100 stars. Moving to SN1987A, a Type II supernova within the LMC, it resulted from the collapse of the a blue supergiant star (SK-69 202). Post-supernova event, a luminous remnant emerged, detectable across multiple spectra, including X-rays, radio waves, and visible light. The variations in UV behavior stem from the interaction between the supernova shock and the circumstellar material, giving rise to a circumstellar ring encompassing the supernova. Our modeling approach included the consideration of 20 UV-emitting stars (O and B type) within a $6'$ radius surrounding the supernova, in conjunction with the UV-emitting circumstellar ring, to effectively simulate the diffuse locations around SN1987A.

The intrinsic FUV luminosities emitted by these sources, including RMC 136 across the 7 FUSE bands, were derived using the Castelli-Kurucz Stellar Atmosphere Model [211] for appropriate spectral type and scaling the results to the observed visual magnitude using the formula [212]:

$$\frac{\Upsilon K_{5500}}{4\pi r^2} \times e^{-\tau_v} = 3.64 \times 10^{-9} \times 10^{-V/2.5} \tag{5.2}$$

Here, Υ stands for the correction factor relating to the star's radius, K_{5500} signifies the Kurucz flux at 5500 Å, τ_v represents the optical depth in the visible wavelength, r denotes the distance measured in centimeters, and V corresponds to the visual magnitude of the star.

For the RMC 136 cluster, computations for its luminosity across all the wavelength bands were conducted using the parameters $R_v = 4.5$ [198, 213], $E(B-V) = 0.29$ [97], $V_{NGC2070} = 7.25$ [SIMBAD], and $r = 1.54 \times 10^{23}$ cm, with results presented in Table 5.2. Similarly, the UV luminosity across all 7 *FUSE* wavelengths for the remaining 20 stars in the SN1987A location was determined using the same methodology, taking into account $E(B-V) = 0.18$ and $R_v = 3.2$ [204]. However, estimation of the UV luminosity for the SN1987A circumstellar ring was not achievable through the stellar atmosphere model. Instead, the study by [214], focusing on the SED of the supernova remnant, was employed. The UV/optical luminosity of the equatorial circumstellar ring, a primary contributor to the

region's UV characteristics, was approximated to be about 3.8×10^{46} photons s^{-1} $Å^{-1}$ or 6.5×10^{35} ergs s^{-1} $Å^{-1}$ at the time of *FUSE* observation based on the SN1987A light curve.

Dust distribution

This study employs a simplified dust configuration commonly found in optically thick scattering objects, employing dusty slabs (or spheres). The primary focus centers on radiative transfer within a plane-parallel slab, a well-established scenario in radiative transfer theory [215]. The dusty slab, positioned 1 kpc in front of the sources and with a thickness of 1 kpc, aims to illustrate the behavior of photons originating from the sources, undergoing a single scattering event before reaching the detector. The optical depth (τ) of the dust distribution varies with the wavelength of the incoming light, and the average optical depth (τ_{avg}) of the dust medium is calculated based on the mean N(H) value for 30 Doradus, 4.5×10^{21} cm^{-2} across all 7 *FUSE* wavelengths (refer to Table 5.4). A portion of the average optical depth (τ_{avg}) contributes to light scattering (τ_1), while the remainder contributes to its attenuation ($e^{-\tau_2}$). The model determines τ_1 and τ_2 values while keeping 'α' and 'g' constant for each wavelength, offering insights into the dust scattering geometry and optical properties.

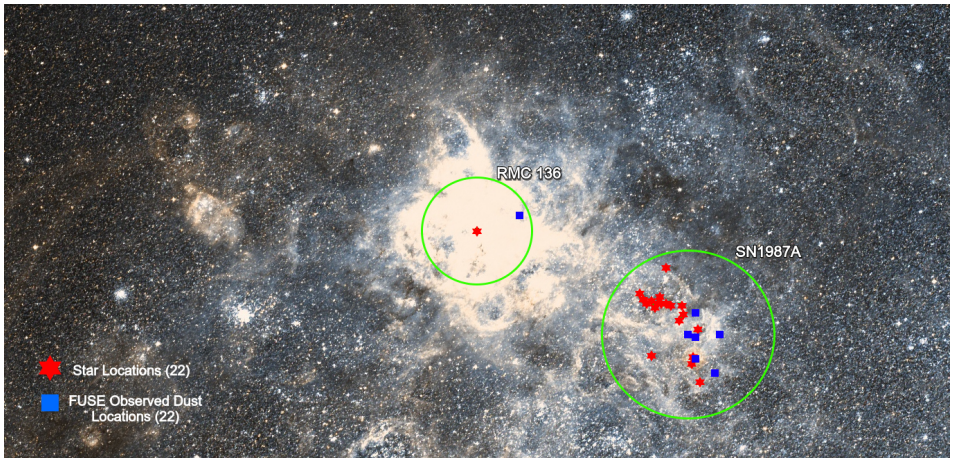

Fig. 5.1 *FUSE* observed dust locations in FUV (blue squares) and the star locations (red stars) overplotted on DSS2 color image of 30 Doradus at field of view of $1.2° \times 36'$

5.4 Results and Discussions

With the input parameters set for the dust model, we proceeded to execute it across the 7 distinct dust locations within 30 Doradus at the 7 *FUSE* wavelengths. This individual analysis produced the best-fit outcomes based on minimum χ^2-statistic, yielding measurements for

Table 5.2 List of the 22 sources under consideration and their luminosities corresponding to the 7 *FUSE* bands (in ergs s^{-1} $Å^{-1}$)

Source Name	gl	gb	Sp. Class	D(Kpc)	V	L_{1004}	L_{1056}	L_{1058}	L_{1112}	L_{1117}	L_{1157}	L_{1159}
RMC 136	279.4651	-31.671889	O7V	50	7.25	9.4E+038	8.9E+038	8.9E+038	7.29E+038	7.29E+038	6.29E+038	6.29E+038
SN 1987A	279.7034	-31.9370	Supernova	50	—	7.52E+035	7.52E+035	7.52E+035	7.52E+035	7.52E+035	7.52E+035	7.52E+035
[WLJ87] Star 2	279.7028	-31.9377	B2III	50	14.88	6.95E+034	7.42E+034	7.42E+034	5.96E+034	5.96E+034	5.70E+034	5.70E+034
[WLJ87] Star 3	279.7036	-31.9366	B2III(Variable)	50	16	2.29E+034	2.46E+034	2.46E+034	1.97E+034	1.97E+034	2.03E+034	2.03E+034
MCPS 083.85193-69.30211	279.7420	-31.9380	B1II-Ib	50	14.07	8.40E+034	9.92E+034	9.92E+034	8.58E+0340	8.58E+034	8.80E+034	8.80E+034
SK-69 203	279.6586	-31.9432	B0.7 Ia	50	12.29	1.59E+036	1.66E+036	1.66E+036	1.39E+036	1.39E+036	1.34E+036	1.34E+036
CPD-69 416	279.59281	-31.8759	BC1 Ia	50	12.16	8.38E+036	8.26E+036	8.26E+036	6.65E+036	6.65E+036	5.91E+036	5.91E+036
UCAC2 1802843	279.6013	-31.8791	B2V	50	13.26	5.82E+035	5.86E+035	5.86E+035	4.78E+035	4.785E+035	4.47E+035	4.47E+035
[ST92]2-67	279.6079	-31.8823	B1V	50	13.9	5.51E+035	5.42E+035	5.42E+035	4.40E+035	4.40E+035	3.99E+035	3.99E+035
SK-69 212	279.6093	-31.8901	O6 If	50	12.42	3.49E+036	3.02E+036	3.02E+036	2.68E+036	2.68E+036	2.36E+036	2.36E+036
[ST92]2-51	279.6094	-31.8914	O7V	50	14.9	4.02E+035	3.80E+035	3.80E+035	3.10E+035	3.10E+035	2.69E+035	2.69E+035
[ST92]2-49	279.6124	-31.8934	O9I	50	15.771	1.63E+035	1.51E+035	1.51E+035	1.29E+035	1.29E+035	1.10E+035	1.10E+035
[M2002]LMC 164299	279.6102	-31.8963	B0I	50	14.068	7.59E+034	7.71E+034	7.71E+034	6.54E+034	6.54E+034	5.85E+034	5.85E+034
BREY 58	279.6168	-31.9254	O3If*/WN6	50	14.13	5.16E+036	4.90E+036	4.90E+036	3.67E+036	3.67E+036	3.14E+036	3.14E+036
BREY 57	279.6026	-31.9006	WN7ha+OB	50	13.486	7.14E+036	6.47E+036	6.47E+036	5.29E+036	5.29E+036	4.76E+036	4.76E+036
HD 269828	279.6109	-31.9011	WN7+O3	50	13.031	4.39E+036	3.96E+036	3.96E+036	3.34E+036	3.34E+036	2.92E+036	2.92E+036
[ST92]2-31	279.6127	-31.9074	B1V	50	16.054	1.04E+035	1.07E+035	1.07E+035	7.93E+034	7.93E+034	7.81E+034	7.81E+034
[ST92]2-28	279.6170	-31.9126	O7V	50	14.318	6.86E+035	6.51E+035	6.51E+035	5.33E+035	5.33E+035	4.62E+035	4.62E+035
UCAC2 1802717	279.6418	-31.9371	O8V	161	14.96	1.43E+036	1.37E+036	1.37E+036	1.12E+036	1.12E+036	9.59E+035	9.59E+035
2MASS J05354059-6912517	279.6359	-31.9258	O8V	50	15.632	1.88E+035	1.79E+035	1.79E+035	1.46E+035	1.46E+035	1.26E+035	1.26E+035
[M2002] LMC 163970	279.5558	-31.9128	O9V	50	14.666	4.50E+035	4.37E+035	4.37E+035	3.55E+035	3.55E+035	3.03E+035	3.03E+035
MCPS 084.03213-69.26608	279.6904	-31.8794	O5V((f))z	26.31	13.87	3.43E+035	3.21E+035	3.21E+035	2.58E+035	2.58E+035	2.23E+035	2.23E+035

Table 5.3 *FUSE* observed dust scattered intensities (in photons cm^{-2} s^{-1} sr^{-1} $Å^{-1}$) [96]

Locations	gl	gb	1A1	1A2	1B1	1B2	2A1	2A2	2B1
L1	279.4483	-31.7298	65400	105600	154100	149500	190800	167500	105600
L2	279.6674	-31.9327	39900	53500	57100	67100	61100	57800	53300
L3	279.7035	-31.9359	199000	261200	313200	312700	317000	299300	233200
L4	279.6685	-31.9398	45600	70900	94900	105600	104000	89200	57300
L5	279.6334	-31.9436	22200	34600	50300	50300	59700	51700	34600
L6	279.7307	-31.9579	15300	22400	19000	22600	14300	16100	17300
L7	279.6734	-31.9714	45600	62300	53200	65200	56700	57700	47700

Table 5.4 *FUSE* wavelengths and corresponding albedo (α), asymmetry factor (g), extinction cross section (σ_{ext} (in cm^2 / H) [35] and calculated mean optical depth (τ_{avg})

FUSE Wavelengths(Å)	Albedo(α)	Asymmetry(g)	σ_{ext}	τ_{avg}
1004(1A1)	0.2306	0.6257	7.2625E-22	3.26
1056(2B1)	0.2465	0.6307	6.5605E-22	2.95
1058(1A2)	0.2465	0.6307	6.5605E-22	2.95
1112(2A2)	0.2580	0.6379	6.0650E-22	2.70
1117(1B1)	0.2594	0.6387	6.0000E-22	2.70
1157(1B2)	0.2684	0.6425	5.7930E-22	2.50
1159(2A1)	0.2700	0.6424	5.6400E-22	2.53

both the scattering optical depth (τ_1) and attenuation optical depth (τ_2) at each location (refer to Table 5.5 and Table 5.6). Furthermore, our investigation also focused on determining the contribution of RMC 136 to the observed scattered FUV emission at 1157 Å across all dust locations. The results highlighted the pivotal role of the cluster as the primary source driving the FUV diffuse emissions.

The wavelength dependence of the scattered light intensity provides a sensitive probe of the optical depth of the scattering medium [216]. The *FUSE* wavelengths and the scattering optical depth (τ_1) corresponding to the dust locations are tabulated in Table 5.8.

The outcomes from the single scattering model depict an alignment between the observed values and a moderately thick optical depth in the FUV wavelength range. The scattering optical depths (τ_1) observed, ranging between 0.71 to 1.77 (see Table 5.5), imply a complex and heterogeneous dust geometry across different locations within the H II region. This variability likely stems from diverse factors like dust density, distribution patterns, and particle sizes. These findings suggest that in diffuse locations, a portion of FUV photons scatter off the outer layer of the dust cloud, while the remaining energy contributes to thermal excitation of dust grains. The FUV penetration in a molecular cloud depends on aspects such

Table 5.5 Single scattering model outputs for the *FUSE* bands (Continued in Table 5.6)

1004 Å, α = 0.2306, g = 0.6257, $\sigma_{ext} = 7.2600 \times 10^{-22}$, $\tau_{avg} = 3.2625$					
Dust Location	τ_1	τ_2	Observed Intensity	Model Intensity	% error
L1	0.8091	2.4534	65400	65600	0.3058
L2	1.4648	1.7976	39900	39756	0.3611
L3	0.8971	2.3653	199000	198887	0.0567
L4	1.4518	1.8106	45600	45498	0.2236
L5	1.0962	2.1663	22200	22239	0.1756
L6	1.1875	2.0749	15300	15396	0.6274
L7	1.7715	1.4909	45600	45483	0.2565
1056 Å, α = 0.2465, g = 0.6307, $\sigma_{ext} = 6.5605 \times 10^{-22}$, $\tau_{avg} = 2.95$					
Dust Location	τ_1	τ_2	Observed Intensity	Model Intensity	% error
L1	0.7482	2.1518	105600	105422	0.1685
L2	1.305	1.595	53300	53462	0.3040
L3	0.7105	2.1895	233200	234227	0.4403
L4	1.247	1.653	57300	57348	0.0837
L5	1.015	1.885	34600	34308	0.8439
L6	0.928	1.9720	17300	17183	0.6763
L7	1.4645	1.4355	47700	47538	0.3396
1058 Å, α = 0.2465, g = 0.6307, $\sigma_{ext} = 6.5605 \times 10^{-22}$, $\tau_{avg} = 2.95$					
Dust Location	τ_1	τ_2	Observed Intensity	Model Intensity	% error
L1	0.7480	2.1520	105600	105421	0.1670
L2	1.3485	1.5515	53500	53177	0.6037
L3	0.8352	2.0650	261200	262398	0.4586
L4	1.4181	1.4819	70900	70841	0.0832
L5	1.0875	1.8125	34600	34833	0.6734
L6	1.1310	1.7690	22400	22360	0.1785
L7	1.6675	1.2325	62300	62830	0.8507
1112 Å, α = 0.2580, g = 0.6379, $\sigma_{ext} = 6.065 \times 10^{-22}$, $\tau_{avg} = 2.74$					
Dust Location	τ_1	τ_2	Observed Intensity	Model Intensity	% error
L1	0.9891	1.7108	167500	166416	0.6471
L2	1.3206	1.3793	57800	57269	0.9186
L3	0.8083	1.8917	299300	297975	0.4426
L4	1.4850	1.2149	89200	89530	0.3699
L5	1.2357	1.4642	51700	51591	0.2108
L6	0.8932	1.8067	16100	16037	0.3913
L7	1.1656	1.1656	57700	57415	0.4939
1117 Å, α = 0.2594, g = 0.6387, $\sigma_{ext} = 6.00 \times 10^{-22}$, $\tau_{avg} = 2.70$					
Dust Location	τ_1	τ_2	Observed Intensity	Model Intensity	% error
L1	0.9315	1.7685	154100	154482	0.2478
L2	1.2960	1.4040	57100	57407	0.5376
L3	0.8100	1.8900	313200	312200	0.3192
L4	1.5552	1.1448	94900	94529	0.3909
L5	1.1988	1.5012	50300	50255	0.0894
L6	0.9558	1.7442	19000	19126	0.6631
L7	1.4607	1.2393	53200	53235	0.0657

Table 5.6 Single scattering model outputs for the *FUSE* bands (Contd.)

1157 Å, α = 0.2684, g = 0.6425, $\sigma_{ext} = 5.70 \times 10^{-22}$, $\tau_{avg} = 2.5$					
Dust Location	τ_1	τ_2	Observed Intensity	Model Intensity	% error
L1	0.84	1.66	149500	149014	0.3250
L2	1.275	1.225	67100	67376.3	0.4117
L3	0.7125	1.7875	312700	312366	0.1068
L4	1.4325	1.0675	105600	10181	0.3968
L5	1.1025	1.3975	50300	50353	0.1048
L6	0.9450	1.3975	22600	22594	0.2292
L7	1.4700	1.0300	65200	65205	0.0082
1159 Å, α = 0.2684, g = 0.6425, $\sigma_{ext} = 5.64 \times 10^{-22}$, $\tau_{avg} = 2.53$					
Dust Location	τ_1	τ_2	Observed Intensity	Model Intensity	% error
L1	0.9640	1.5660	190800	190270	0.2777
L2	1.2321	1.2978	61100	61101	0.0011
L3	0.7235	1.8064	317000	316223	0.2451
L4	1.4395	1.0904	104000	104571	0.5490
L5	1.2017	1.32825	59700	59394	0.5125
L6	0.7412	1.7887	14300	14240	0.4195
L7	1.4041	1.12585	56700	56996	0.5220

Table 5.7 Percentage contribution of RMC 136 to the surface brightness of the diffuse FUV emission at dust locations at 1157 Å

Location	Observed Flux	Model Flux	% contribution
L1	149500	148248	99.2
L2	67100	40402	60.2
L3	312700	12343	3.9
L4	105600	52420	49.6
L5	50300	29743	59.1
L6	22600	19530	86.4
L7	65200	52823	81.0

Table 5.8 Scattering optical depth (τ_1) of each dust location corresponding to the *FUSE* wavelengths (μm^{-1})

$1/\lambda(\mu^{-1})$	L1	L2	L3	L4	L5	L6	L7
9.9601	0.8091	1.4648	0.8971	1.4518	1.0962	1.18755	1.7715
9.4696	0.7482	1.3050	0.7105	1.2470	1.0150	0.9280	1.4645
9.4517	0.7480	1.3485	0.8352	1.4181	1.0875	1.131	1.6675
8.9928	0.9891	1.3206	0.8083	1.4850	1.2357	0.8932	1.5344
8.9525	0.9315	1.2960	0.8100	1.5552	1.1988	0.9558	1.4607
8.6430	0.8400	1.2750	0.7125	1.4325	1.1025	0.9450	1.470
8.6281	0.9639	1.2321	0.7235	1.4396	1.2017	0.7412	1.4041

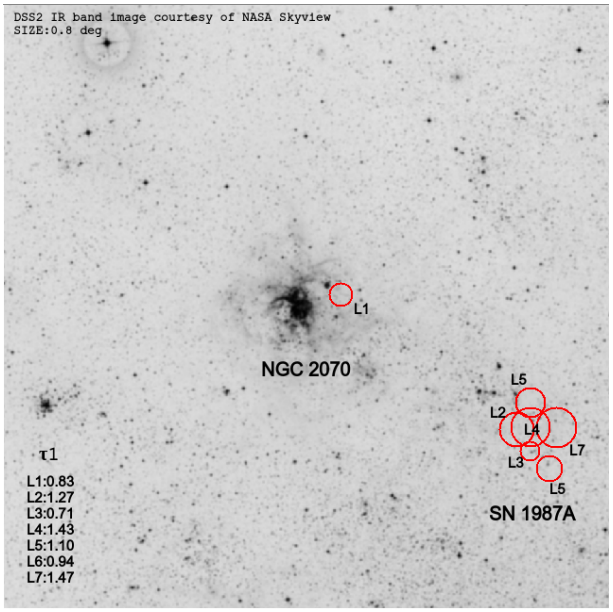

Fig. 5.2 The scattering optical depth (τ_1) (1157 Å) at the 30 Doradus *FUSE* locations is represented by circles. The area of the circles is proportional to τ_1. These circles are overlaid on a DSS2 IR band image

as dust albedo (α) and radiation anisotropy (g), where higher α and g values usually indicate deeper FUV penetration [217]. Notably, areas with higher FUV scattered intensity (like L1 and L3 in our study) demonstrated lower scattering optical depths. This could indicate either sparser dust density or a more transparent medium to FUV radiation. This scenario might suggest that FUV radiation penetrates deeper into the medium before encountering significant scattering interactions.

5.5 Conclusions

This study effectively applied a single scattering model to closely replicate the observed dispersed FUV light in the 30 Doradus H II region. It unveiled a complex dust structure, predominantly optically thick, responsible for scattering FUV light. A minor fraction of FUV photons scatter off the thin outer dust layers, while the bulk of them interact with dust grains, and get thermally re-emitted. To enhance our understanding of dust grain properties and the dust geometry in the 30 Doradus region, our future work will include modeling the diffuse FUV emission alongside the thermally re-emitted MIR and FIR emissions using different multiple scattering models.